Original Research

Investigation of the Processes Involved in the Formation of Pyroxene Materials during Solar Melting in a Large Solar Furnace

Muhammad S. Paizullakhanov [1], Feruza A. Giyasova [2], Khayot N. Bakhronov [3], Murodjon A. Yuldoshev [4,*], Alisher A. Mamadaliev [2], Farkhod A. Giyasov [2], Feruza T. Akbarova [5], Bakhtiyor Ismatov [6], Mira R. Bekchanova [7]

[1] Institute of Materials Science of the Academy of Sciences of the Republic of Uzbekistan, Tashkent 100047, Uzbekistan;
[2] Department of Energy and Applied Sciences, Kimyo International University in Tashkent, Tashkent 100121, Uzbekistan;
[3] Department of Physics, Tashkent University of Information Technologies named after Muhammad al-Khwarizmi, Tashkent 100084, Uzbekistan;
[4] Department of Scientific Department, Turan International University, Namangan 160106, Uzbekistan
[5] Department of Physics, Namangan State Technical University, Namangan 160100, Uzbekistan;
[6] Department of Engineering Graphics and Design Theory, Tashkent Institute of Irrigation and Agricultural Mechanization Engineers National Research University, Tashkent 100000, Uzbekistan;
[7] Department of Natural Sciences, University of Public Security of the Republic of Uzbekistan, Tashkent 100211, Uzbekistan
* Correspondence: murod.yuldoshev1993@gmail.com

Received: December 3, 2025; Accepted: January 26, 2026

Abstract: The study investigates the influence of the parameters of concentrated light radiation (CLR) and the melt-cooling conditions on the structure formation, phase composition, and properties of pyroxene glass-ceramics. It is established that quenching the melt in water results in the formation of an amorphous glass, whereas reducing the cooling rate (~100 °C/s) leads to partial crystallization with the formation of diopside and augite phases. An increase in CLR flux density from 100 to 300 W/cm² promotes a higher degree of crystallinity, transitioning from a diopside–augite mixture to a monomineralic diopside–hedenbergite phase $Ca(Fe,Mg)Si_2O_6$. Increasing the flux density and the melt holding time is accompanied by an increase in apparent density (from ~2.70 to ~2.90 g/cm³) and a decrease in abrasion loss (from ~0.018 to ~0.008 g/cm³), indicating enhanced densification and wear resistance of the material. Optimal CLR conditions (≈300 W/cm², ~10³ °C/s) ensure the formation of a dense, homogeneous microstructure with low water absorption (0.02 %), high wear resistance (0.006 g/cm²), and a flexural strength of ≈145 MPa. The obtained results confirm the promise of pyroxene glass-ceramics for applications requiring thermally stable and wear-resistant materials.

Keywords: solar furnace; melt synthesis; pyroxene; flux density; wear resistance

1. Introduction

It is well known that the physicochemical properties of materials are largely determined by the synthesis method employed and follow the relationship: “synthesis method – morphology – properties” [1]. One of the most widely used approaches is solid-state synthesis, the principle of which consists in heating a substance or a mixture of starting components to temperatures below their melting point (approximately 0.5÷0.7 T_m) [2]. Under these conditions, the chemical interaction between components proceeds predominantly through the diffusion of atoms [3] of one or both

reacting substances through the layer of solid reaction products. The diffusion coefficients in such processes typically range from 10^{-12} to 10^{-10} cm²/s, which results in comparatively low reaction rates in the solid state [4]. Consequently, long synthesis durations are required and, as a result, the final product often exhibits a heterogeneous structure and phase composition [5].

In recent years, the field of materials science associated with the study of melt-quenching processes has undergone intensive development, driven by efforts to obtain materials with a favorable combination of physicochemical and performance properties [6]. Melts represent a distinct aggregate state of matter at temperatures above the melting point. Their structure is characterized by a combination of cluster formations, in which atoms are arranged in a partially ordered manner close to their positions in the crystal lattice, and an intercluster region with a predominantly disordered atomic organization. It is believed that the granular structure inherited by the melt from the initial solid state can be largely preserved and transferred to the new solid material formed during subsequent crystallization. In this context, clusters represent stable atomic groupings whose size is significantly smaller than that of typical crystalline nuclei [7,8]. If a liquid that has inherited structural features from the solid state is overheated to the point of transitioning into a structureless (simple) liquid, it loses all characteristic features of its initial structural organization. It should be noted that the structure of melts may also be influenced by external factors. For example, ultrasonic treatment or even mechanical stirring can contribute to the refinement of the melt's granular structure, whereas the application of an alternating magnetic field leads to modulation of grain boundaries, facilitating the movement of atoms along intergranular regions and thus improving flow behavior [9,10]. The use of sensible heat retained in the molten state makes it possible to significantly reduce energy consumption compared with conventional heat-treatment methods [11]. Typically, melt quenching is carried out from temperatures of about 1450 °C, after which the resulting product is used as a raw material for the production of cement and concrete, which generally exhibit relatively low performance characteristics [12,13].

In recent years, particular attention has been paid to glass-ceramic materials formed by melt quenching followed by two-stage heat treatment, including stages of internal nucleation and growth of crystalline phases [14]. Such materials are characterized by high mechanical strength (ultimate bending strength up to 150-300 MPa) [15], increased heat resistance and a low coefficient of linear thermal expansion ($\alpha \sim 10^{-6}$ K^{-1}) [16], which significantly exceeds the performance of traditional natural and building materials, including granite and marble. The combination of these properties makes glass-ceramic materials highly promising for specialized and highly loaded applications. In particular, sitalls - glass-crystalline materials - are widely used in conditions requiring a combination of high mechanical strength, thermal and chemical resistance, including radio electronics (microcircuit substrates and insulating elements), aerospace technology (fairings and structural components), the chemical industry (pipelines and protective coatings), and instrument making [17,18].

In this context, one of the key technological parameters determining the quality of the melt being formed is the rate at which the initial material is heated to and above its melting temperature, as well as the rate of subsequent cooling. It has been noted that the use of solar technologies opens fundamentally new possibilities for controlling these processes: by concentrating solar radiation, it becomes possible to increase heating rates by several orders of magnitude and to produce melts of high chemical purity, characterized by cluster structures of a specific composition. The application of rapid and ultrarapid quenching methods under such conditions enables the fixation of metastable states and facilitates the production of materials with a unique set of properties.

The development of modern energy systems and the enhancement of efficiency in materials-science processes are directly linked to the expanded use of renewable energy sources, among which solar energy holds a particularly prominent position. In recent decades, there has been a growing interest in the synthesis of materials with high mechanical and dielectric properties through the methods of directional crystallization of melts generated using heliothermal installations [19]. A particularly promising direction in solar technology is the development of materials based on pyroxene structures $CaMgSi_2O_6$. Unlike conventional thermal energy sources, solar furnaces make it

possible to substantially increase heating rates and thereby enable the production and stabilization of melts with tailored cluster architectures. This, in turn, creates favorable conditions for obtaining materials with predictable performance characteristics, including enhanced mechanical and dielectric properties, making this approach highly relevant for a wide range of engineering and energy applications [20].

The aim of this study is to perform a comprehensive analysis of the physicochemical processes occurring during the heating, melting, and subsequent cooling of pyroxene materials, as well as of the $CaMgSi_2O_6$ (diopside) crystalline structures obtained from the melt in a solar furnace (SF) under varying flux densities of concentrated solar radiation (CSR).

2. Experimental Samples and Research Methods

In the present work, pyroxene structures of calcium–magnesium silicate ($CaMgSi_2O_6$) were investigated, obtained using technogenic waste represented by basaltic rocks from tungsten skarns. The pyroxene samples were synthesized according to the following technological scheme: grinding of the initial components → mixing → shaping → melting → quenching [21]. The synthesis of pyroxene phases was carried out by melting the prepared batch in a CSR flux using a solar furnace (SF) with a vertical optical axis [22].

The synthesis was performed at a temperature of 1600 °C, with a heating rate of 1100 °C/min. Melting of the materials was conducted in the Large Solar Furnace (LSF) on a water-cooled substrate within a CSR flux range of 100÷350 W/cm² [23, 24]. The CSR flux density was calculated on the basis of the Stefan–Boltzmann equation, which describes the radiation of heated bodies [25]:

$$Q=\varepsilon\sigma T^4 \quad (1)$$

where, ε is the emissivity of the material, $\sigma=5.67\times10^{-8}$ W/m²·K⁴ is the Stefan–Boltzmann constant, and T is the temperature of the body (K). The flux density at the focal spot of the SF during the experiments was monitored using a FLIR E5-XT Wi-Fi thermal imager. As determined, the density of the concentrated flux incident on the crucible containing the material was at least 120 W/cm² and remained stable within ±5%. Quenching of the melt was carried out either by water cooling (v_{cool} ~10^3 °C/s) or by solidification on the water-cooled surface where melting occurred (v_{cool} ~10^2 °C/s). When the raw material was held under a flux density of at least 150 W/cm² for 20 minutes, the most complete melting was observed. At a flux density of 300 W/cm², the resulting glasses were more homogeneous. Glass synthesis was also performed using a radiation-heating installation (URAN) and in an electric furnace chamber.

X-ray phase analysis of the investigated samples was performed using an Empyrean diffractometer (PANalytical) in Bragg–Brentano reflection geometry with Cu Kα radiation (wavelength λ=1.5418 Å). The scanning range was $20 \le 2\theta \le 60°$. The diffractometer slit system was adjusted to ensure complete coverage of the sample by the X-ray beam across the entire working 2θ range. Reference tables by J.H. Kittel [26] were used for the processing and interpretation of the obtained diffractograms. The X-ray density was calculated using the expression $\rho_x=1.66\times M/V$, where M is the formula unit mass in grams, and V is the unit cell volume in Å³. The relative density was determined as $(\rho_{app}/\rho_x) \times 100\%$, where $\rho_{app}=m/V$ corresponds to the apparent density, calculated as the ratio of the sample mass (m, g) to its volume (V, cm³).

3. Results and Discussion

An important step in obtaining pyroxene materials with predetermined properties is the selection of raw materials and their quantitative ratios in accordance with the required stoichiometric composition [27,28]. Calculations were carried out for the monomineralic pyroxene phase of composition $CaMgSi_2O_6$, taking into account the molar ratios of $CaO:MgO:SiO_2$ corresponding to the formula unit of diopside. For each component, the mass fractions were determined to achieve a ratio close to stoichiometric, which allows the formation of pyroxene structures with minimal content of secondary phases during melting and subsequent quenching [29]. Table 1 presents the calculated

values for the starting components, their conversion to oxide composition, and the final ratios corresponding to the monomineralic pyroxene composition.

Table 1. Calculation of raw materials for obtaining a monomineralic pyroxene composition ($CaMgSi_2O_6$).

Oxides	Wt. %	Molar Amount	Normative baseline groups								Deficient SiO_2, CaO, MgO		Pyroxene Composition	
			Al_2O_3 $2SiO_2K_2O$	Al_2O_3 $2SiO_2Na_2O$	$CaOAl_2O_3TiO_2$	$2Al_2O_3$ $CaOSiO_2$	$CaOFeOSiO_2$	Fe_2O_3 $CaOSiO_2$	MgO $CaOSiO_2$	$CaOSiO_2$	Мол.кол	Wt. %	Wt. %	Recalculated to 100%
SiO_2	44.1	0.73	0.024	0.012		0.02	0.05	0.018	0.064	0.54	0.07	4.56	48.6	40.8
TiO_2	0.8	0.01			0.006								0.48	0.40
Al_2O	9.21	0.09	0.012	0.024	0.006	0.04							9.21	7.73
Fe_2O_3	2.87	0.02						0.018					2.87	2.41
MgO	2.57	0.064							0.064		0.15	6.08	8.65	7.26
CaO	31.2	0.55			0.006	0.02	0.05	0.018	0.064	0.54	0.15	8.52	39.7	33.3
K_2O	1.90	0.02	0.012										1.9	1.59
FeO	6.11	0.08					0.05						6.11	5.13
Na_2O	1.52	0.02		0.024									1.52	1.27

For the raw materials with the given chemical composition, the pyroxene module was 3.24, which exceeds the standard threshold value corresponding to the onset of pyroxene formation (3.0) [30]. This indicates a deviation from the optimal stoichiometric ratio of the components and necessitates adjustment of the batch. To achieve the desired monomineralic pyroxene composition, the calculation included additional batching in the form of dolomite (as a source of calcium and magnesium) and silicon oxide, which allowed balancing the ratio of oxide components and ensured the formation of the $CaMgSi_2O_6$ phase (Table 1).

It is known that glass-ceramics are formed during the recrystallization of the glass mass upon the introduction of specific catalysts that promote complete or partial crystallization of the material. The degree of melt superheating and the cooling rate have a significant impact on this process [31,32]. The structural and performance characteristics of glass-ceramics depend on the chemical composition of the initial glass, the type and concentration of the catalyst, as well as the parameters of thermal treatment. Glass-ceramics are characterized by a microcrystalline structure, in which a glassy phase is uniformly distributed between small crystals measuring approximately 2-8 μm; in highly crystallized materials, its content reaches 5-10 %. Therefore, one of the key tasks in the synthesis of glass-ceramic materials is determining the optimal technological conditions for obtaining a diopside structure, taking into account the value of the pyroxene module.

Melting was carried out in a SP on a water-cooled substrate at a flux density of 100-350 W/cm². Quenching of the melt was carried out in two ways: by rapid cooling in water (~10^3 °C/s) or by solidification on a water-cooled substrate on which melting occurred (~10^2 °C/s). It was found that when the raw material was irradiated with a flux of at least 150 W/cm² for 20 min, the most complete

melting of the material was observed. With an increase in flux density to 300 W/cm², the resulting glasses were characterized by higher homogeneity [33]

To assess the influence of the spectral composition of the radiation on the glass synthesis process, experiments were conducted by melting various materials under focused solar flux, using a radiation-heating installation (URAN), as well as in an electric furnace chamber. The melting results are presented in Table 2, showing the dependence of material characteristics on the type of installation: T_m—melting temperature (°C), E_g—bandgap width (eV), ε—blackness factor, and Q—required CSR flux density (W/cm²). The obtained data allow evaluating the effect of energy spectral distribution on the efficiency of melting and the formation of the glassy phase.

Table 2. Results of material melting depending on the type of furnace.

Materials	**T_m, ºC**	**E_g, eV**	**ε**	**Q, W/cm²**	**Result**		
					SF	**URANUS**	**Electric oven**
Fe_2O_3	1390	2.2	0.8	43	++	++	+
Pyroxene	1390		0.85	43	++	++	+
SiO_2	1550	5.7	0.73	63	-	-	+
TiO_2	1870	3 – 3.2	0.78	120	+	+	-
$BaCO_3$	2293		0.70	247	-	-	-
CaO	2614	7	0.93	394	-	-	-
MgO	2825		0.72	522	-	-	-
Note	«-» no melting «+» – melting, «++» – complete melting						

A comparison of spectral characteristics showed that the concentrated flux in the focal zone of the solar furnace (SF) covers a wavelength range from 0.3 to 3 μm, providing a broad spectrum of energy impact on the material. At the same time, the radiation of the URAN solar spectrum simulator exhibits a more complex distribution: approximately 9% of the energy falls within the ultraviolet region, 35% within the visible, 40% within the near-infrared range (0.8–1 μm), and 16% within the far-infrared range (λ>1 μm). In electric furnaces with resistance heaters, the spectral composition of the radiation is determined by the temperature of the heated bodies and is described by the relationship λ=2980/T (μm), indicating a predominant contribution of infrared radiation to the thermal exposure process [34].

Considering the above, the high sensitivity of glasses to melting and cooling conditions necessitates analyzing the influence of the KSI flux density and melt cooling rate on the glass-ceramic formation processes and the development of the material's functional characteristics. In this regard, Figure 1 presents X-ray diffraction patterns of glass-ceramics obtained from glasses synthesized at different KSI flux densities, clearly demonstrating the influence of energy processing parameters on the phase composition and degree of crystallinity.

Under conditions of a flux density of 100 W/cm² and a cooling rate of approximately 10^3 °C/s, partial crystallization of the initial glass is observed, with the formation of silicate phases of the diopside-augite type, characteristic of the early stage of structural ordering of the glass-ceramic material. X-ray phase analysis (Figure 1) of the synthesized sample confirms the formation of predominantly crystalline phases of diopside ($CaMgSi_2O_6$) and augite ($(Ca,Mg,Fe)_2(Si,Al)_2O_6$), with the main crystalline phase corresponding to augite-type pyroxene with a diopside structure. The diffraction pattern of the obtained material is characterized by intense and well-resolved diffraction maxima in the range of 2θ=20–65°, while pronounced peaks at 2θ=25–40° indicate a high level of crystallinity, and a background increase in intensity at small angles (2θ < 25°) indicates the presence

of an amorphous phase, which is typical for incompletely crystallized sitalls [35,36]. The relatively low intensity of the diffraction maxima demonstrates incomplete structural rearrangement, which is due to the limited thermodynamic conditions of synthesis [37–39].

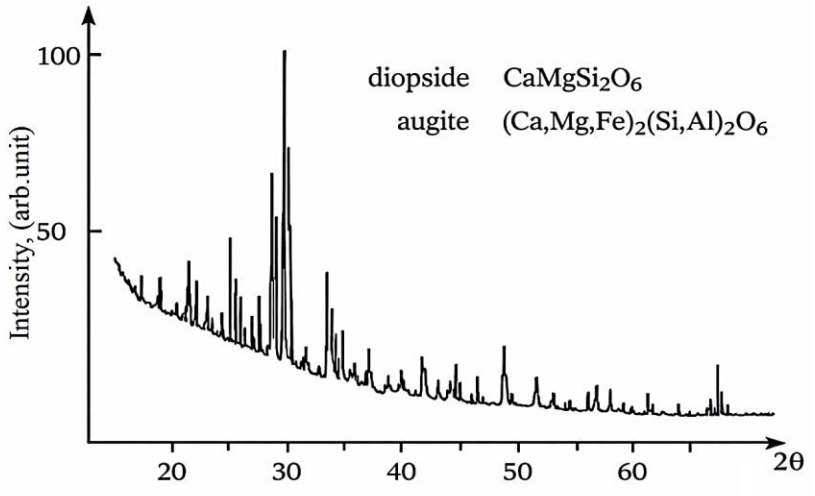

Figure 1. X-ray diffraction spectra of glass-ceramics synthesized at a KSI flux density of 100 W/cm², with identification of diopside and augite phases.

The phase identification and indexing of diffraction maxima were performed within the monoclinic crystallographic system. The structure of the sample is described by the space group C2/c, characteristic of augite and diopside, and the parameters of the unit cell crystallizing in this syngony were determined using the generalized equation for interplanar distances [40]:

$$\frac{1}{d^2} = \frac{h^2}{a^2} + \frac{k^2 sin^2\beta}{b^2} + \frac{l^2}{c^2} + \frac{2hl\cos\beta}{ac} \quad (2)$$

The interplanar distance d was calculated according to Bragg's law [40]:

$$n\lambda = 2d\sin\theta \quad (3)$$

where, n=1, λ is the wavelength of X-ray radiation, θ is the Bragg angle.

The unit cell parameters of diopside ($CaMgSi_2O_6$) and augite ($(Ca,Mg,Fe)_2(Si,Al)_2O_6$) obtained as a result of X-ray diffraction analysis correspond to the literature data [41], which confirms the formation of a stable crystal structure of clinopyroxenes without pronounced crystallographic distortions. For the diopside phase, the following unit cell parameters were established: a ≈ 9.73 Å, b ≈ 8.92 Å, c ≈ 5.24 Å, monoclinic angle β ≈ 105.6°, with a calculated cell volume of V ≈ 439.4 Å³. The crystallographic parameters of augite are characterized by the following values: a ≈ 9.78 Å, b ≈ 8.83 Å, c ≈ 5.26 Å, β ≈ 106.3°, V ≈ 435.98 Å³. The observed variations in the parameters compared to pure diopside are explained by the isomorphic substitution of cations in the crystal lattice of the mineral. A slight increase in the parameters a and b compared to ideal diopside may be associated with the isomorphic substitution of Mg^{2+} ions by Fe^{2+}/Fe^{3+} ions in octahedral positions, which leads to a local expansion of the crystal lattice. The preservation of the characteristic monoclinic angle β ≈ 105–106° confirms the structure belongs to the monoclinic pyroxene type and the absence of phase transitions. The main diffraction maxima were successfully indexed, further confirming the single-phase nature of the material. The absence of extraneous reflections within the sensitivity of the method indicates the completion of phase formation processes and the appropriateness of the chosen synthesis conditions. The calculated unit cell parameters, as well as the results of indexing the main diffraction reflections of augite and diopside, are presented in Table 3.

Table 3. Crystallographic parameters and diffraction peak indexing results for augite and diopside

№	2θ, degree		Interplanar distance d, Å		Miller indices (hkl)	
	Augite	Diopside	Augite	Diopside	Augite	Diopside
1	20.1	19.9	4.41	4.46	(020)	(020)
2	27.8	27.6	3.21	3.23	(220)	(111)
3	29.9	29.8	2.986	2.99	(221)	($\bar{2}$21)
4	31.2	30.8	2.87	2.89	(310)	(220)
5	35.6	35.5	2.527	2.53	(002)	(311)
6	36.8	35.8	2.46	2.51	($\bar{2}$21)	($\bar{3}$11)
7	40.8	40.6	2.23	2.21	($\bar{3}$11)	(131)
8	42.6	42.2	2.12	2.14	(400)	(330)
9	50.8	52.7	1.81	1.74	($\bar{4}$02)	(151)
10	60.3	62.1	1.54	1.50	(512)	(060)

As can be seen from Table 3, in the region of medium and high diffraction angles (2θ > 35°), clearly resolved reflections with interplanar distances d ≈ 2.53-1.50 Å are recorded, indexed by planes (002), ($\bar{2}$21), ($\bar{3}$11), (400), ($\bar{4}$02) and (512) for augite and (311), ($\bar{3}$11), (131), (330), (151) and (060) for diopside; The presence and unambiguous indexing of these reflections confirm the formation of a crystallographically ordered three-dimensional crystalline structure of both phases without signs of significant distortions or amorphous inclusions, while the proximity of the 2θ and d values for the corresponding reflections indicates their structural relationship and belonging to the clinopyroxene type, and the identified differences reflect the features of the cationic composition and the degree of isomorphic substitution [42].

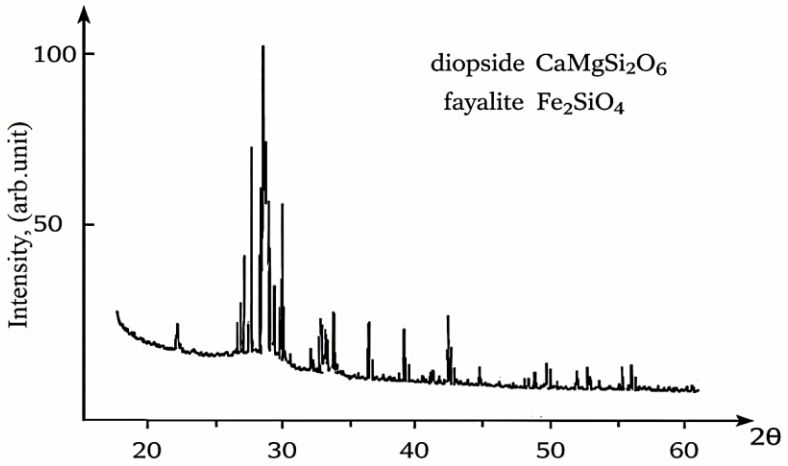

Figure 2. X-ray diffraction spectra of sitalls synthesized at a KSI flux density of 200 W/cm², with identification of diopside and feyalite phases.

The X-ray diffraction pattern (Figure 2) of a sitall sample sintered from glass at a flux density of 200 W/cm² shows the formation of a more ordered crystalline structure compared to the material obtained at 100 W/cm². The diffraction pattern is characterized by narrow and intense diffraction peaks of the diopside ($CaMgSi_2O_6$) and fayalite (Fe_2SiO_4) phases, reflecting the high crystallographic ordering of the material. The enhancement of peaks in the range of 2θ = 25–40° demonstrates an increase in the degree of crystallinity and the predominance of silicate phases. The decrease in the amorphous background relative to the previous sample reflects the development of structural

ordering processes in the bulk of the material. Exposure to a flux density of 200 W/cm² leads to active crystallization processes and the formation of a stable multiphase system with a predominance of diopside and fayalite components, which improves the structural integrity and phase stability of sitalls [43,44]. Based on the position and relative intensities of reflections, it was revealed that the sample is a two-phase system including $CaMgSi_2O_6$ and Fe_2SiO_4. Additional diffraction lines corresponding to impurity or amorphous phases were not detected in the studied angular range, which indicates a high phase purity of the synthesized material. The most intense peak in the diffraction pattern is observed at $2\theta \approx 29.9°$, which is characteristic of diopside and corresponds to reflection from the (221) plane. The interplanar distance d, calculated using Bragg's law (3) at $\theta = 14.95°$, is ≈ 2.98 Å and is within the literature data [41] for monoclinic $CaMgSi_2O_6$. Other characteristic reflections of diopside, recorded at $2\theta \approx 31.1°, 35.6°, 49.9°$ and 60.1°, were indexed as (310), (002), (150) and (440), respectively.

Fayalite crystallizes in the orthorhombic syngony (space group P_{nma}) with rhombic symmetry, demonstrating close packing and a significantly smaller unit cell volume (307.6 Å³), the parameters of which were calculated using the expression [45]:

$$\frac{1}{d^2} = \frac{h^2}{a^2} + \frac{k^2}{b^2} + \frac{l^2}{c^2} \quad (4)$$

The obtained lattice parameters were: a ≈ 4.82 Å, b ≈ 10.48 Å, c ≈ 6.09 Å.

The unit cell parameters and indexing of the main diffraction peaks of Fe_2SiO_4 are presented in Table 4.

Table 4. Diffraction characteristics of the main phases of Fe_2SiO_4

№	2θ, degree	Interplanar distance d, Å	Miller indices (hkl)
1	18.2	4.87	(020)
2	29.3	3.05	(111)
3	31.1	2.87	(021)
4	35.4	2.53	(121)
5	37.0	2.43	(130)
6	41.7	2.16	(002)
7	47.1	1.93	(220)
8	49.6	1.84	(040)
9	57.2	1.61	(042)
10	62.9	1.48	(242)

Table 4 shows how the contribution of the Fe_2SiO_4 phase manifests itself in the 2θ range ≈ 33–35° and 41–57°, where reflections corresponding to the (130), (040), and (242) planes are observed. Minor deviations may be due to isomorphic substitution of Mg^{2+} and Fe^{2+} ions, as well as microstrains and residual stresses arising during synthesis and heat treatment. Narrow and symmetrical diffraction peaks confirm a high degree of structural order and a minimal number of defects in the crystal lattice.

The X-ray diffraction pattern (Figure 3) of the glass-ceramic material obtained from glass at a flux density of 300 W/cm² demonstrates the formation of an ordered crystalline structure. The diffraction pattern clearly shows intense peaks corresponding to the diopside-hedenbergite phase $Ca(Fe,Mg)Si_2O_6$, indicating the predominance of a monomineral composition. The increase in the intensity of the maxima in the range of $2\theta = 28–35°$ and the decrease in the amorphous background reflect the almost complete crystallization, stabilization of the lattice, and the transition of the melt to a homogeneous structural state [46,47]. Exposure to a 300 W/cm² ISR promotes directional crystal growth and the formation of a stable diopside-hedenbergite phase, increasing structural order and improving the physical and mechanical properties of the material. X-ray diffraction analysis

confirmed that the sample belongs to the monoclinic syngony (space group C2/c) and showed that the most intense peak at 2θ ≈ 30° corresponds to the interplanar distance d ≈ 2.97 Å and is indexed as (221). The calculated unit cell parameters and its volume are consistent with the literature data [48] and reflect the isomorphic substitution of Mg^{2+} by Fe^{2+} ions in octahedral positions. The diffraction pattern shows narrow and clearly defined peaks in the range of 2θ ≈ 18–65°, indicating a high degree of crystallographic ordering. The shift of the peaks towards smaller angles is due to the partial substitution of Mg^{2+} by Fe^{2+} ions and an increase in the unit cell parameters, and the relative intensities reflect the orientation of atomic planes and SiO_4 chains in the structure. The diopside-hedenbergite structure is described by a monoclinic cell with the parameters: a ≈ 9.9 Å, b ≈ 9.1 Å, c ≈ 5.3 Å, V ≈ 447 $Å^3$, β ≈ 106.5°. Table 3 below shows the indexing of the main diffraction reflections of $Ca(Fe,Mg)Si_2O_6$ in the range 2θ = 18–65°.

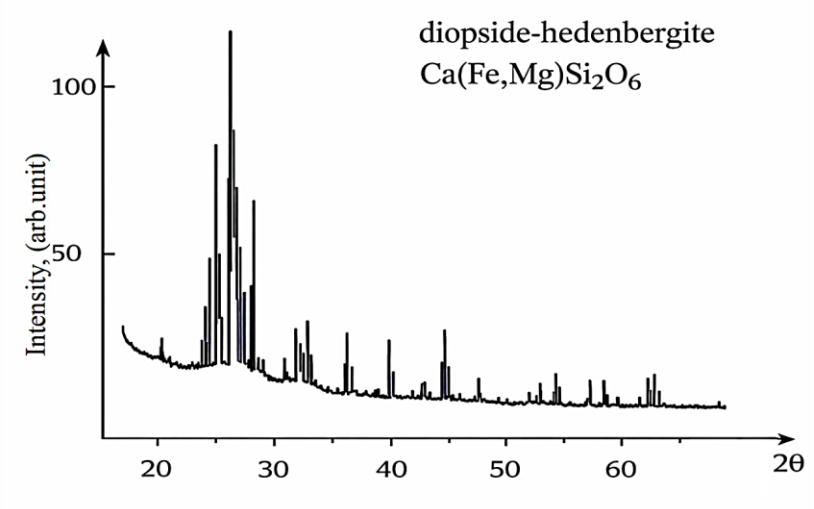

Figure 3. X-ray diffraction spectra of glass-ceramics synthesized at a KSI flux density of 300 W/cm², with identification of diopside-hedenbergite phases.

From the diffraction characteristics of the main reflections of the $Ca(Fe,Mg)Si_2O_6$ phase presented in Table 5, it follows that the successive decrease in interplanar distances with an increase in the diffraction angle, up to d = 1.47 Å at 2θ = 63.4° for the (461) plane, corresponds to Bragg's law and reflects the regularity of the crystal lattice, while the presence of clearly indexed reflections (240), (330), (202), (152), (352) and (052), the parameters of which are consistent with literary data [41], confirms the stability of the structure and indicates the potential of the material for further studies of its physicochemical and functional properties.

Table 5. Diffraction characteristics of the main phases of $Ca(Fe,Mg)Si_2O_6$.

№	2θ, degree	Interplanar distance d, Å	Miller indices (hkl)
1	18.1	4.90	(110)
2	29.9	2.98	(221)
3	31.2	2.86	(310)
4	35.1	2.55	(240)
5	39.5	2.28	(330)
6	41.3	2.18	(202)
7	46.8	1.94	(152)
8	54.6	1.68	(352)
9	59.1	1.56	(052)
10	63.4	1.47	(461)

With increasing CSR flux density, the degree of single-phase material also increases: as the energy flux density rises, secondary phases gradually disappear, indicating improved structural homogeneity of the melt. The physico-mechanical characteristics of sintered pyroxene materials obtained from glasses formed at different flux densities vary significantly. It has been observed that increasing the flux density and the holding time of the melt leads to an increase in the apparent density of the material (Figures 4 and 5), indicating intensification of densification processes and the formation of a more homogeneous microstructure [49].

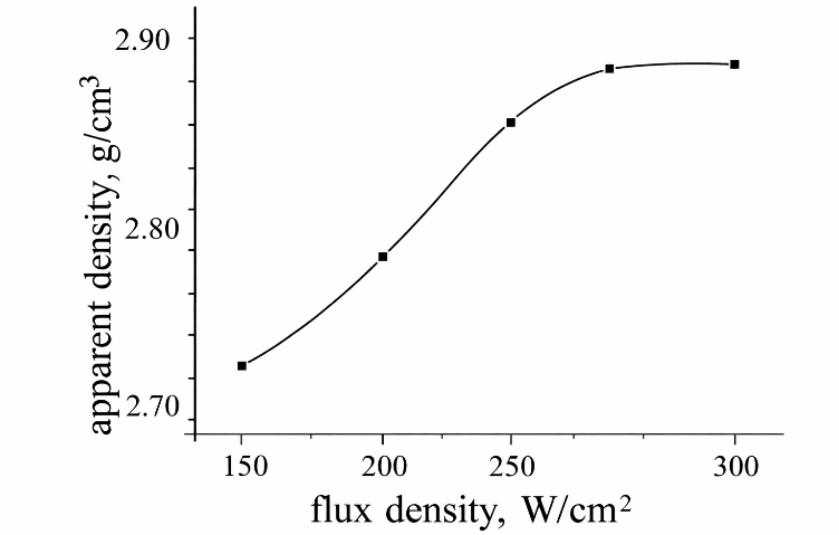

Figure 4. Dependence of the apparent density of the pyroxene material on the flux density (~10^3 °C/s).

Based on the presented graph (Figure 4) showing the dependence of the apparent density of the pyroxene material on CSR flux density (~10^3 °C/s), it was established that increasing the flux density from 150 to 300 W/cm² leads to a monotonic increase in apparent density from ~2.70 to ~2.90 g/cm³. This trend indicates the intensification of densification processes and a reduction in material porosity under higher energy exposure. In the range of 250-300 W/cm², the rate of density increase slows, indicating that a maximum level of structural ordering has been reached and densification processes have become saturated. The obtained results confirm that increasing the flux density promotes the formation of a more homogeneous microstructure and reduces the number of defects in the pyroxene material [50].

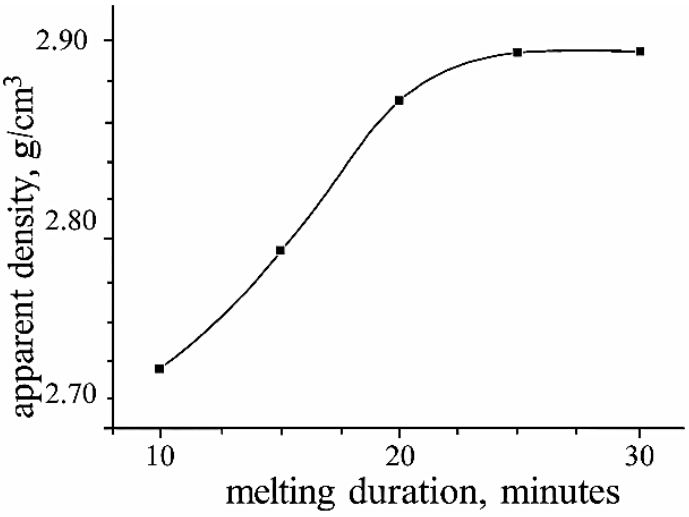

Figure 5. Dependence of the apparent density of the pyroxene material on the melt holding time (300 W/cm², ~10^3 °C/s).

From the dependence shown in Figure 5 of the apparent density of the pyroxene material on melt holding time (30 min) at a flux density of 300 W/cm² and a cooling rate of ~10³ °C/s, it was established that increasing the holding time from 10 to 25 minutes leads to an increase in apparent density from ~2.70 to ~2.90 g/cm³. This dependence exhibits a saturation behavior: after 25–30 minutes, the material density reaches its maximum value, indicating the completion of degassing and densification processes. The initial density increase during the early stage of melting is attributed to the intensification of melt homogenization and reduction of porosity. Further extension of holding time does not lead to significant changes in density, indicating that a thermodynamically stable state of the melt and an equilibrium phase distribution in the pyroxene material have been achieved [51].

CSR flux density also significantly affected the wear resistance of the materials (Figure 6), as well as their mechanical strength and deformation under load.

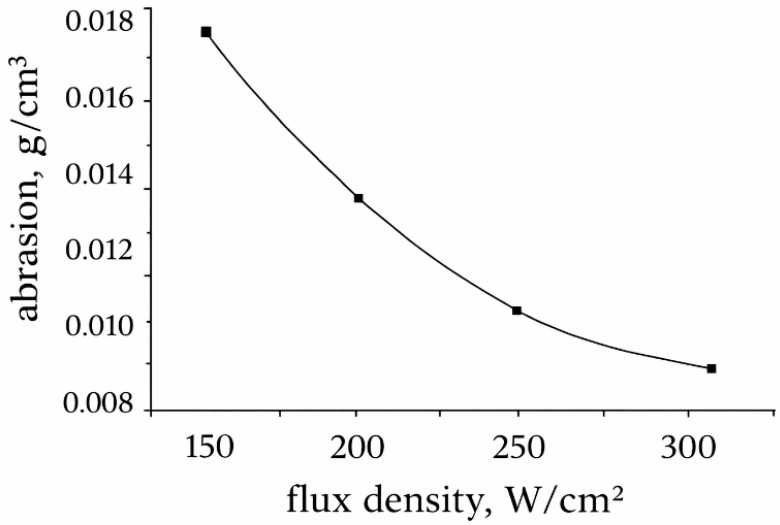

Figure 6. Dependence of the wear resistance of the pyroxene material on the flux density (~10³ °C/s).

From the dependence shown in Figure 6 of the wear resistance of the pyroxene material on flux density at a heating rate of ~10³ °C/s, it was found that increasing the flux density from 150 to 300 W/cm² leads to a pronounced decrease in wear loss, from ~0.018 to ~0.008 g/cm³. This trend indicates an enhancement of the material's wear resistance under more intensive thermal exposure. The reduction in wear loss is likely associated with increased density and structural homogeneity due to more complete sintering of particles and a decrease in the number of defects and pores. At flux densities above 250 W/cm², the decrease in wear loss slows, indicating that optimal conditions for forming a dense, stable microstructure of the pyroxene material have been reached [52,53].

Water absorption and flexural strength of pyroxene glass-ceramic samples synthesized at different flux densities (Table 6) show a clear correlation with the intensity of concentrated light radiation, demonstrating a significant influence of the synthesis energy parameters on the structural and mechanical properties of the material [54].

Table 6. Properties of sintered pyroxene glass-ceramic materials depending on CSR flux density.

Parameters	**Flux Density, W/cm²**			
	150	**200**	**250**	**300**
Water absorption, %	0.05	0.04	0.03	0.02
Bending strength, MPa	125	130	140	145
Wear Loss, g/cm²	0.018	0.012	0.008	0.006

As can be seen from the data (Table 6), increasing the flux density leads to partial disruption of the crystalline order, resulting in a decrease in the fraction of regions with ordered atomic structure and an increase in the proportion of amorphous areas. In this context, the glassy phase acts as a buffer medium, facilitating the relaxation of stresses arising during crystal growth and limiting their development, which determines the quantitative ratio of crystalline phases and the material's porosity [55]. An increase in the fraction of crystalline phases and a reduction in grain size contribute to the enhancement of the mechanical strength of the glass-ceramic material.

High CSR flux densities promote the formation of a homogeneous melt and the directional crystallization of a monomineralic diopside–hedenbergite structure [56]. This, in turn, ensures a higher degree of structural ordering and underlies the improved mechanical properties of the resulting glass-ceramic materials (Table 7).

Table 7. Degree of amorphousness of sintered pyroxene glass-ceramic material.

Synthesis Conditions							
In the Solar Furnace (SF)				**In the Electric Furnace**			
Flux Density, W/cm²	150	200	300	Temperature, °C	1450	1600	1800
Degree of Amorphousness	8	14	22	Degree of amorphousness	5	12	18

To ensure the formation of homogeneous glass, the synthesis should be carried out at radiative flux densities that provide significant superheating of the melt, in the range of 300÷350 W/cm². At lower flux densities, careful control of the heating rate is required, as its reduction leads to slower phase transformations in the silicate system and increases the temperature and duration of the final stage of heat treatment [57]. Comparative analysis of the effects of different types of radiation on the melting process showed that the degree of amorphousness of the resulting material is strongly dependent on the nature of the energy exposure. Thus, during glass synthesis in a solar furnace, the degree of amorphousness is higher than when using electric heating, reaching approximately 22%.

4. Conclusions

The conducted studies demonstrated that quenching the melt in water results in the formation of amorphous glass, characterized by a broad maximum on the X-ray diffraction pattern in the $2\theta \approx 20–35°$ region, indicating the absence of crystalline phases. Reducing the cooling rate to ~100 °C/s leads to partial crystallization, with the formation of diopside $CaMgSi_2O_6$ and augite $Ca(Mg,Fe)Si_2O_6$ phases, as evidenced by narrow peaks in the $2\theta \approx 25–45°$ range.

Based on X-ray phase analysis, it was established that increasing the CSR flux density enhances the degree of crystallinity of the glass-ceramics and alters their phase composition. At 100 W/cm², diopside–augite phases with an amorphous component are formed; at 200 W/cm², an ordered multiphase structure (diopside, fayalite) develops; and at 300 W/cm², nearly complete crystallization occurs, resulting in the formation of the diopside–hedenbergite phase $Ca(Fe,Mg)Si_2O_6$. Higher flux densities promote directional crystallization and stabilization of the glass-ceramic structure. Increasing the CSR flux density from 150 to 300 W/cm² and holding the melt for 25–30 minutes leads to an increase in the apparent density of the pyroxene material from ~2.70 to ~2.90 g/cm³, reflecting the intensification of densification and structural homogenization processes.

Simultaneously, wear loss decreases from ~0.018 to ~0.008 g/cm³, indicating enhanced wear resistance and improved material strength. Optimal CSR parameters (≈300 W/cm², ~10^3 °C/s) ensure the formation of a dense, homogeneous, and mechanically stable microstructure of pyroxene glass-ceramics. The resulting glass-ceramics exhibit enhanced physico-mechanical properties: water absorption – 0.02%, wear loss – 0.006 g/cm², and flexural strength ≈145 MPa, confirming high density, low porosity, and a well-developed degree of structural ordering.

Acknowledgments: We would like to express our sincere gratitude to everyone who supported us during the preparation of this manuscript. We also thank the peer reviewers for their valuable comments and constructive suggestions, which helped improve the quality of this work.

Availability of Data availability: We confirm that we can provide data upon reasonable request.

Funding: No funding received.

Author Contributions: FAG, MRB and BI: Performed the experimental work; MSP: Writing – original draft, investigation, data curation; MAY: Supervision, funding acquisition, conceptualization; FAG: Writing – review & editing; KhNB: Analysis and interpretation of results; AAM and FTA: Study conception and design, methodology, editing.
All authors contributed to the critical revision of the manuscript for important intellectual content.
All authors read and approved of the final manuscript.
All authors have participated sufficiently in the work and agreed to be accountable for all aspects of the work.

Conflicts of Interest: All authors certify that they have no conflicts of interest or professional relationships that might inappropriately affect the results presented in this research.

References

1. Huan, S.; Liu, G.; Han, G.; et al. Effect of Experimental Parameters on Morphological, Mechanical and Hydrophobic Properties of Electrospun Polystyrene Fibers. *Materials* 2015, 8(5), 2718–2734. https://doi.org/10.3390/ma8052718
2. Yadav, A.K. A Review on Synthesis Methods of Materials Science and Nanotechnology. *Advanced Materials Letters* 2024, 15(3), 24031758. https://doi.org/10.5185/amlett.2024.031758
3. Rondón, J.; Lizardo, A.G.; Bravo, R.; et al. Solid-State Diffusion: An Introduction. *Materials Science* 2024, 17662. https://doi.org/10.48550/arXiv.2407.17662
4. Chen, B.; Jiang, T.; Zhou, M.; et al. Interdiffusion kinetics and solid-state reaction mechanism between Cr2O3 and calcium ferrite based on diffusion couple method. *Journal of Alloys and Compounds* 2021, 865, 158754. https://doi.org/10.1016/j.jallcom.2021.158754
5. Sosso, G.C.; Behler, J.; Bernasconi, M. Breakdown of Stokes-Einstein relation in the supercooled liquid state of phase change materials. *Physica status solidi (b)* 2012, 249(10), 1880–1885. https://doi.org/10.1002/pssb.201200355
6. Xu, X.L.; Hou, H.; Liu, F. Rapid Solidification of Undercooled Melts. In Solidification. IntechOpen; 2018, pp. 23–42. https://doi.org/10.5772/intechopen.70666
7. Sharibaev, N.Yu.; Ergashov, A.Q.; Fazliddinov, S.B.; et al. Photoelectric characteristics of TiO_2-based on thin-film solar elements with ruthenium (II) compounds. *Journal of Ovonic Research* 2025, 21(6), 859. https://doi.org/10.15251/JOR.2025.216.859
8. Jiang, A.L.; Li, Y.J.; Wu, Q.H.; et al. Structure Models of Metal Melts: A Review. *Materials* 2024, 17(23), 5882. https://doi.org/10.3390/ma17235882
9. Kong, W.; Cang, D.Q. Effects of ultrasound on the flow field in molten steel and solidification structure. *SIMULATION* 2011, 88(6), 694–706. https://doi.org/10.1177/0037549711422248
10. Hu, W.; Le, Q.; Liao, Q.; et al. Effects of Ultrasonic Treatment on Grain Refinement and Gas Removal in Magnesium Alloys. *Crystals* 2024, 14(3), 237. https://doi.org/10.3390/cryst14030237
11. Zhao, Y.; Chen, D.; Bi, Y.; et al. Preparation of low cost glass–ceramics from molten blast furnace slag. *Ceramics International* 2012, 38(3), 2495–2500. https://doi.org/10.1016/j.ceramint.2011.11.018
12. Qin, Y.; Lv, X; Bai, C.; et al. Waste Heat Recovery from Blast Furnace Slag by Chemical Reactions. *JOM* 2012, 64(8), 997–1001. https://doi.org/10.1007/s11837-012-0392-3
13. Gomes, V.; De Borba, C.D.G.; Riella H.G. Production and characterization of glass ceramics from steelwork slag. *Journal of Materials Science* 2002, 37(12), 2581–2585. https://doi.org/10.1023/A:1015468329645
14. Hu, A.; Li, M.; Mao, D. Controlled crystallization of glass–ceramics with two nucleating agents. *Materials Characterization* 2009, 60(12), 1529–1533. https://doi.org/10.1016/j.matchar.2009.09.001
15. Honma, T.; Maeda, K.; Nakane, S.; et al. Unique properties and potential of glass-ceramics. *Journal of the Ceramic Society of Japan* 2022, 130(8), 545–551. https://doi.org/10.2109/jcersj2.22037
16. Bach, H., Krause, D. *Low Thermal Expansion Glass Ceramics*, 2nd ed. Springer 2005. pp. 248. https://doi.org/10.1007/3-540-28245-9

17. Utamuradova, Sh.B.; Azamatov, Z.T.; Popov, A.I.; et al. Study of optical, electrophotographic and holographic parameters of As-Se condensates from the prehistory of the original bulk materials. *East European Journal of Physics* 2024, 3, 278–281. https://doi.org/10.26565/2312-4334-2024-3-27
18. Chainikova, A.S.; Voropaeva, M.V.; Alekseeva, L.A.; et al. Current state of developments in the field of radio-transparent cordierite glass-ceramics (review). *Aviation Materials and Technologies* 2014, 6, 45–51. https://doi.org/10.18577/2071-9140-2014-0-s6-45-51
19. Manankov, A.V.; Gasanova, E.R.; Bikova, V.V. Physico-chemical and technological aspects of the development of new class sitalls. *Proceedings of the Voronezh State University of Engineering Technologies* 2018, 80(1), 211–222. https://doi.org/10.20914/2310-1202-2018-1-211-222
20. Rumi, M.Kh.; Nurmatov, Sh.R.; Mansurova, É.P.; et al. Materials for surface protection of heating boiler tubes. *Glass and Ceramic* 2017, 74, 172–175. https://doi.org/10.1007/s10717-017-9955-7
21. Zanotto, E.D.; Mauro, J.C. The Glassy State of Matter: Its Definition and Ultimate Fate. *Journal of Non-Crystalline Solids* 2017, 471, 490–495. https://doi.org/10.1016/j.jnoncrysol.2017.05.019
22. Payzullakhanov, M.S.; Akbarov, R.Yu.; Shermatov, Zh.Z.; et al. Small Solar Furnace for Processing and Melting of Materials. Actual Problems of the Energy Complex: Production, Transmission and Ecology, In: Proceedings of the Collection of Materials of the International Scientific and Technical Conference; 25–26 April 2024; Karshi, Uzbekistan. P. 533–538.
23. Abdurakhmanov, A.A.; Akbarov, P.Yu.; Akhadov, Zh.Z.; et al. Creating Melting Furnaces Based on the Large Solar Furnace. *Applied Solar Energy* 2008, 44(4), 284–287. https://doi.org/10.3103/S0003701X08040129
24. Klychev, Sh.I.; Bakhramov, S.A.; Parpiev, O.R.; et al. Optical-Energy Characteristics and Heating Temperatures in Small Single-Mirror Solar Furnaces. *Applied Solar Energy* 2025, 60(5), 703–707. https://doi.org/10.3103/S0003701X24602394
25. Duffie, J.A.; Beckman, W.A. Solar Engineering of Thermal Processes, 4th ed. John Wiley & Sons; 2013. https://doi.org/10.1002/9781118671603
26. Kittel, J.H. *Table of Interplanar Spacings for Crystal-Structure Determinations by X-Ray Diffraction With Molybdenum, Copper, Cobalt, Iron, and Chromium Radiations.* National advisory committee for aeronautics: Washington, DC, USA, 1945; pp. 62.
27. Shelby, J.E. Introduction to Glass Science and Technology, 2nd ed. Royal Society of Chemistry; 2005. pp. 138-168. https://doi.org/10.1039/9781839169229
28. Bakhronov, Kh.; Ergashev, O.; Ochilov, G.; et al. Study of Isotherm, Thermodynamic Characteristics and Sorption Mechanism of Toluene Adsorption on Zeolite CsZSM-5 by Adsorption-Calorimetric Method. *Edelweiss Applied Science and Technology* 2024, 8(6), 6959–6966. https://doi.org/10.55214/25768484.v8i6.3508
29. Paizullakhanov, M.S.; Atabaev, I.G.; Fayziev, Sh. The Glass Ceramics Pyroxene Composition Synthesized on the Solar Furnace. *Australian Mining* 2016. https://doi.org/10.20431/2454-9460.0202002
30. Zvyagin, B.B.; Merlino, St. The Pyroxene-Spinel Polysomatic System. *Zeitschrift für Kristallographie* 2003, 218(3), 210–220. https://doi.org/10.1524/zkri.218.3.210.20747
31. Li, J.; Lai, F.; Yao, W.; et al. Effects of the Cooling Rate on the Crystallization Behaviors of the CaO-Al_2O_3-B_2O_3-CaF_2-Based Mold Flux. *CrystEngComm* 2020, 22(12), 2158–2165. https://doi.org/10.1039/C9CE01931F
32. Dong, W.; Lu, J.S.; Feng, Z.J.; et al. Effect of Glass Cooling Rate on the Crystallization Behavior and Structure of Lithium Aluminosilicate Glass-ceramics. *Journal of Inorganic Materials* 2012, 27(4), 400–404. https://doi.org/10.3724/SP.J.1077.2012.00400
33. Silveira, W.D.; Macedo, W.C.; Santos, G.T.D.A; et al. Crystallization Kinetics and Structure Refinement of $CaTiO_3$ Glass-Ceramics Produced by Melt-Quenching Technique. *Materials Research* 2021, 24(Suppl 1), e20210027. https://doi.org/10.1590/1980-5373-MR-2021-0027
34. Paizullakhanov, M.S.; Sulaymonov, M.; Holmatov, A.; et al. Features of Glass Produced from a Solar Furnace. *Chemistry and Chemical Engineering* 2024, 2022(2), Article 4. https://doi.org/10.70189/1992-9498.1515
35. Paizullakhanov, M.S. The Glass Crystalline Materials Synthesized in the Solar Furnace. *Computational nanotechnology* 2016, 2. 106–112.
36. Rakhmanov, S.; Matchonov, K.; Yusupov, H.; et al. Optical High Harmonic Generation in Dirac Materials. *The European Physical Journal B* 2025, 98, 35. https://doi.org/10.1140/epjb/s10051-025-00885-7
37. Tulyaganov, D.U.; Dimitriadis, K.; Agathopoulos, S.; et al. Glasses and Glass-Ceramics in the CaO-MgO-SiO_2 System: Diopside Containing Compositions—A Brief Review. *Journal of Non-Crystalline Solids* 2023, 612, 122351. https://doi.org/10.1016/j.jnoncrysol.2023.122351

38. Utamuradova, Sh.B.; Giyasova, F.A.; Bakhronov, K.N.; et al. Current Transfer Mechanism in a Thin-Based Heterosystem Based on A_2B_6 Compounds. *East European Journal of Physics* 2025, 3, 325–335. https://doi.org/10.26565/2312-4334-2025-3-31
39. Parpiev, O.R.; Paizullakhonov, M.S.; Nodirmatov, E.Z.; et al. Prospects of Extracting Metals from Technogenic Wastes Using Concentrated Solar Radiation. *Metallurgist* 2022, 66(2). https://doi.org/10.1007/s11015-022-01349-4
40. Arlt, T.; Angel, R.J.; Miletich, R.; et al. High-Pressure $P2_1/c$-C2/c Phase Transitions in Clinopyroxenes; Influence of Cation Size and Electronic Structure. *American Mineralogist* 1998, 83, 1176–1181. https://doi.org/10.2138/am-1998-11-1205
41. Anthony, J.W.; Bideaux, R.A.; Bladh, K.W.; et al. Handbook of Mineralogy, Available online: http://www.handbookofmineralogy.org/ (accessed on 21 October 2025).
42. Rodriguez, E.T.; Anovitz, L.M.; Clement, C.D.; et al. Facile Emulsion Mediated Synthesis of Phase-Pure Diopside Nanoparticles. *Scientific Reports* 2018, 8, 3099. https://doi.org/10.1038/s41598-018-21485-9
43. Kansal, I.; Tulyaganov, D.U.; Goel, A.; et al. Structural Analysis and Thermal Behavior of Diopside–Fluorapatite–Wollastonite-Based Glasses and Glass-Ceramics. *Acta Biomaterialia* 2010, 6(11), 4380–4388. https://doi.org/10.1016/j.actbio.2010.05.019
44. Rusho, M.A.; Ahmed, T.A.; Saleh, L.H.; et al. Design and Synthesis of Decorated Palladium Nanoparticles on Chitosan-Tannic Acid Modified Magnetic Nanoparticles and Evaluation of Its Catalytic Application in the Heck Coupling Reactions. *Journal of Organometallic Chemistry* 2025, 1039, 123773. https://doi.org/10.1016/j.jorganchem.2025.123773
45. Tripoliti, E.K.; Dobson, D.P.; Fortes, A.D.; et al. Structure and Thermal Expansion of End-Member Olivines I: Crystal and Magnetic Structure, Thermal Expansion, and Spontaneous Magnetostriction of Synthetic Fayalite, Fe_2SiO_4, Determined by High-Resolution Neutron Powder Diffraction. *Mineralogical Magazine* 2023, 87, 789–806. https://doi.org/10.1180/mgm.2023.66
46. Ergashev, O.; Bakhronov, Kh.; Giyasova, F.; et al. Energy Characteristics, Adsorption Kinetics, and Mechanism of Triethylamine Adsorption on CsZSM-5 Zeolite. *Journal of Applied Organometallic Chemistry* 2026, 6(1), 43–52. https://doi.org/10.48309/jaoc.2026.546865.1334
47. Zhang, P.; Luo, Z.; Liu, S.X.; et al. Crystallization Kinetics and Optical Properties of Transparent Glass-Ceramics Embedding $ZnGa_2O_4$ Nanocrystals with Enhanced Defect Luminescence. *Journal of Non-Crystalline Solids* 2022, 576, 121255. https://doi.org/10.1016/j.jnoncrysol.2021.121255
48. Huber, A.L.; Heuer, M.; Fehr, K.T.; et al. Characterization of Synthetic Hedenbergite ($CaFeSi_2O_6$)–Petedunnite ($CaZnSi_2O_6$) Solid Solution Series by X-ray Powder Diffraction and ^{57}Fe Mössbauer Spectroscopy. *Phys. Chem. Minerals* 2004, 31, 67–79. https://doi.org/10.1007/s00269-003-0335-1
49. Jiang, K.; Wu, W.; Ren, B.Y.; et al. Highly Crystallized Glass-Ceramics from High Content Gold Tailings via a One-Step Direct Cooling Method. *RSC Advances* 2022, 12(22), 14175–14182. https://doi.org/10.1039/D2RA01012G
50. Talimian, A.; Wondraczek, L.; Galusek, D. Densification of Glass Powder Studied by Master Sintering Curve and Master Kinetic Curve Methods. *International Journal of Applied Glass Science* 2021, 12(4), 541–550. https://doi.org/10.1111/ijag.16232
51. Monich, P.R.; Vollprecht, D.; Bernardo, E. Dense Glass-Ceramics by Fast Sinter-Crystallization of Mixtures of Waste-Derived Glasses. *International Journal of Applied Ceramic Technology* 2019, 17(1), 55–63. https://doi.org/10.1111/ijac.13332
52. Gajek, M.; Rapacz-Kmita, A.; Stodolak-Zych, E.; et al. Microstructure and Mechanical Properties of Diopside and Anorthite Glazes with High Abrasion Resistance. *Ceramics Internationa*l 2022, 48(5), 6792–6798. https://doi.org/10.1016/j.ceramint.2021.11.230
53. Sabirov, K.K.; Yusupov, J.R.; Matyokubov, Kh.Sh.; et al. Networks with Point-Like Nonlinearities. Nanosystems: Phys. Chem. Math. *Наносистемы: физика, химия, математика* 2022, 13(1), 30–35. https://doi.org/10.17586/2220-8054-2022-13-1-30-35
54. Wang, Y.C.; Liu, P.J.; Luo, G.P.; et al. Optimization of Heat Treatment of Glass-Ceramics Made from Blast Furnace Slag. *High Temperature Materials and Processes* 2020, 39(1), 539–544. https://doi.org/10.1515/htmp-2020-0059
55. Kraipok, A.; Mamanee, T.; Ruangsuriya, J.; et al. Phase Formation, Mechanical Strength, and Bioactive Properties of Lithium Disilicate Glass-Ceramics with Different Al_2O_3 Contents. *Materials* (Basel) 2022, 15(23), 8283. https://doi.org/10.3390/ma15238283

56. Kang, B.; Kang, S. Crystal Growth Behavior, Nanometer Microstructure, and Mechanical Properties of Diopside-Based Glass-Ceramics. *Journal of Nanoscience and Nanotechnology* 2020, 20(1), 183–189. https://doi.org/10.1166/jnn.2020.17290
57. Ahmad, S.Q.S.; Wieckert, C.; Hand, R.J. Glass Melting Using Concentrated Solar Thermal Energy. *Glass Technology-European Journal of Glass Science and Technology Part A* 2017, 58(2), 41–48. https://doi.org/10.13036/17533546.58.2.012